

## 6

### Examples of pneumatic structures and material models for membranes

This chapter is divided in two main topics: material models for membranes and static analysis of pneumatic structures. Initially uniaxial and biaxial numerical examples of Ethylene tetrafluoroethylene (ETFE) strips using the material models described and validated in chapter 3 will be presented. The numerical results are compared with experimental data. The second example is a biaxial test of the ETFE strip modeled with the PD–NURBS material model presented in chapter 4.

A pneumatic structure based in the experimental analysis of the inflation of a circular membrane are numerically analyzed. The material of the circular membrane is also the ETFE, which is modeled with the material models of chapter 3.

Analysis of an air cushion with one and two chambers for linear elastic material and pressure–volume coupling are also presented and the results are compared. Finally results for a real size pneumatic structure cushion are presented. By this model, the PD–NURBS material and the pressure-volume coupling are considered. Cutting pattern generation is also performed.

#### 6.1 ETFE–Foils

Growing use of ETFE–Foils in pneumatic structures has motivated the application of the material models presented in this work to ETFE membranes.

ETFE is a polymer classified as a semi-crystalline thermoplastic. This type of polymer is more resistant to solvents and other chemicals.

Ethylene tetrafluoroethylene consists of monomers of Ethylene ( $C_2H_4$ ) and Tetrafluoroethylene ( $C_2F_4$ ). When these monomers are submitted to moderate temperatures, pressures, and in the presence of a catalyst, they polymerizes:

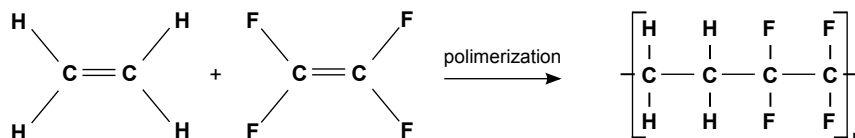


Figure 6.1: Ethylene Tetrafluoroethylene chemical structure

In 1970 an ETFE material was produced for the first time by DuPONT<sup>TM</sup> with the name Tefzel®. The features of Tefzel® are described in the Properties Handbook [54].

According to Robinson-Gayle et al. [80], ETFE was first used as a roofing material in a zoo building in Burgers Zoo, Arnheim in the Netherlands in 1981. It has subsequently been used in various buildings predominantly in the United Kingdom and Germany.

The lightweight of the ETFE foil is one of the most important features that motivate its use in structural buildings. Moreover, it has been used more often in roofs, resulting in low cost for the foundation. Beyond this property of lightweight, ETFE has many other advantageous properties. Tanno [81] listed some:

- Non stick characteristics making it virtually self-cleaning with little need for maintenance.
- Good translucency and light transmission qualities in visible and UV ranges.
- Can be coated to help further in the control of heat and light transmission properties.
- Excellent thermal control properties can be achieved through multi-layer foils.
- Extreme resistance to weathering and excellent resistance to solvents and chemicals.
- Excellent characteristics for fire emergency situations in roofs and atria.
- Linear elastic behavior up to 20 MPa and high elongation without damage.

The translucency property is advantageous, because it allows the utilization of natural light, reducing the use of artificial light. Another property related with resource consumption and commented by Robinson-Gayle et al. [80] is the anti-adhesive nature of ETFE. This property means that roofs and atria need to be cleaned less frequently. This leads to a reduction in the cost of detergents and water to maintain the building.

Recycling is other characteristic that is important in terms of sustainability. Robinson-Gayle et al. [80] points out that once the material is clean it can be recycled by heating it to its softening temperature. The softening temperature of an ETFE is low so this is not a very costly operation. The recycled ETFE can be added into the hopper with virgin ETFE.

Figures 1.5 and 6.2 show some examples of cushion structures with ETFE-foils. The flexibility to create structural forms with this material is highlighted in these examples.



Figure 6.2: Eden Project in the United Kingdom

### 6.1.1 Material Behavior

Barthel et al. [82] carried out biaxial experiments with ETFE-foils and found that the results in both directions show a largely matching material mechanical behavior, in other words, the material behaves almost isotropically. Galliot and Luchsinger [53] performed tensile tests at many angles ( $15^\circ$ ,  $30^\circ$ ,  $60^\circ$  and  $75^\circ$ ) and also gave similar results. The curves are identical and small variations appear in the non-linear domains. They concluded that the extrusion process does not significantly affect the material behavior and that ETFE-foils have almost isotropic behaviour. Because of this, in the present work the assumption of isotropic behavior will be adopted.

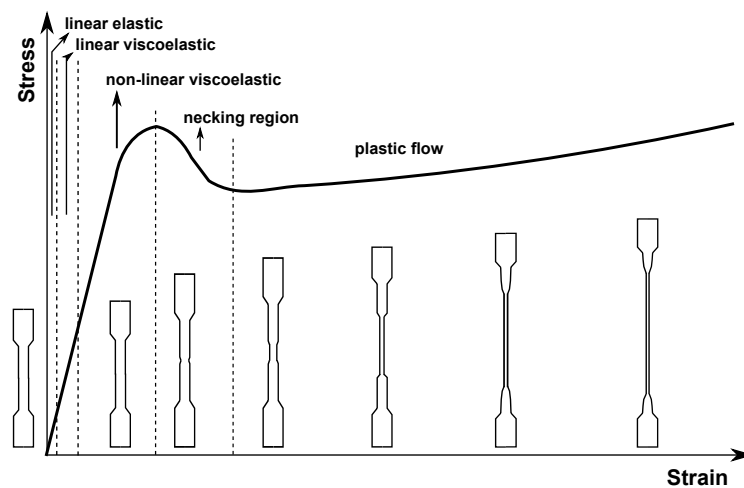


Figure 6.3: Stress–strain curve of semi–crystalline thermoplastic material with schematic representation of the tensile specimen in different steps (source: Ehrenstein [83])

Ehrenstein [83] shows in his work a typical stress–strain curve of semi–crystalline thermoplastic material and this curve is presented in figure 6.3. In the present work two phases are considered: linear elastic and elastoplastic.

Figure 6.4 shows the tensile and compressive stress–strain curve for the ETFE material at a temperature of  $+23^\circ\text{C}$ . The ETFE used in buildings is the Tefzel®200.

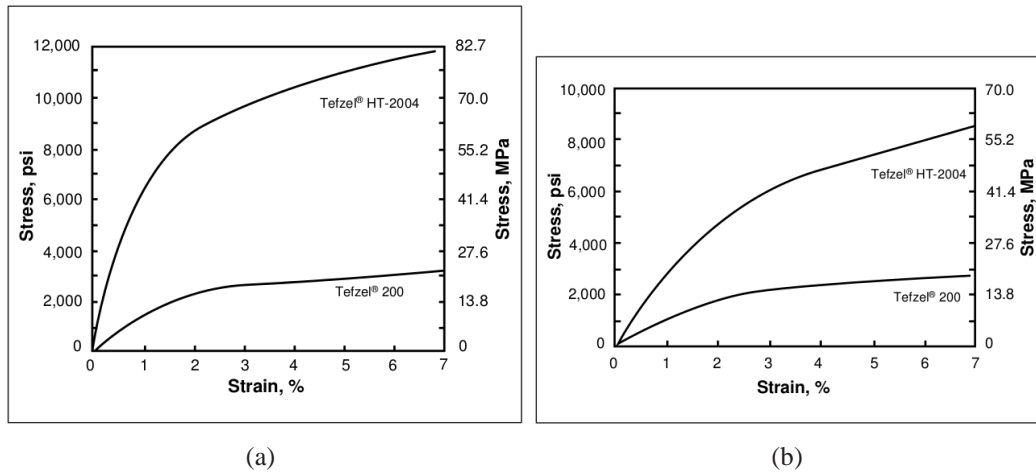


Figure 6.4: Stress–strain curve: (a) tensile stress vs. strain and (b) compressive stress vs. strain (source Properties Handbook of Tefzel®[54])

### 6.1.1.1 Temperature influence

Moritz [15] carried out biaxial experiments in the proportion of 3:1 for different levels of temperature (-25°C, 0°C, +23°C and +35°C). Figure 6.5 presents the results of these experiments. The material is the ASAHI®FLUON ETFE NJ (thickness = 250μm). The right side of the curves (positive strain) are the stress results in axis I and the left side of the curves (negative strain) are the stress results in axis II.

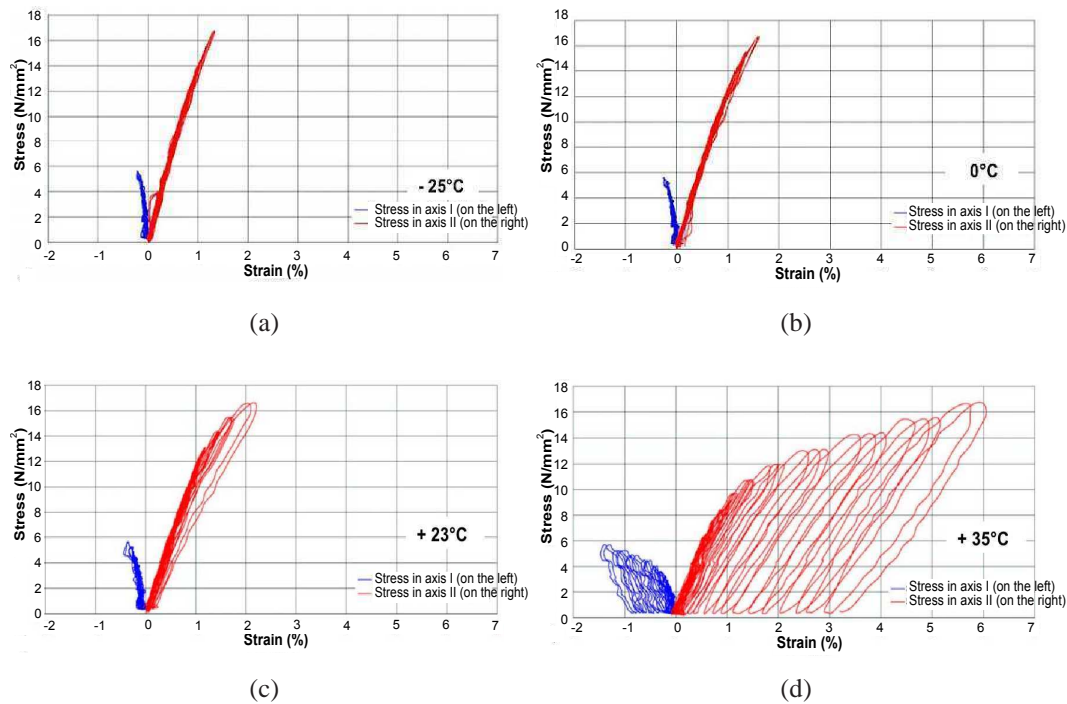


Figure 6.5: Stress–strain curves for cyclic test: (a) -25°C, (b) 0°C, (c) +23°C and (d) +35°C (source: Moritz [15])

The temperature influence by this material is clearly observed in figure 6.5. In figures 6.5(a), 6.5(b), and 6.5(c) the results for the cyclic loading test have reversible strain and stress, indicating elastic behavior. For the temperature of +35°C (figure 6.5(d)) a residual strain is observed, indicating plastic behavior.

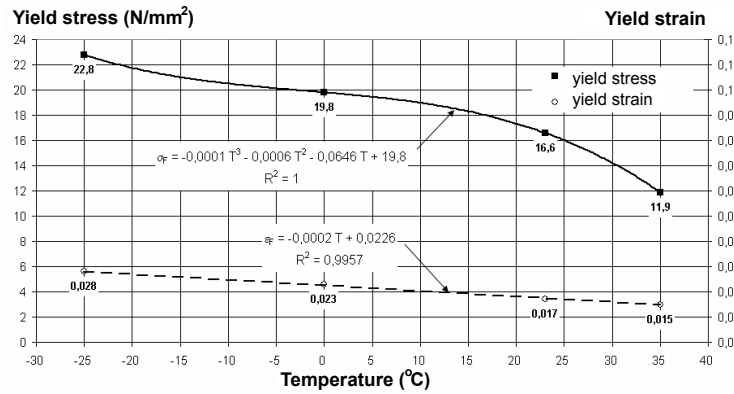
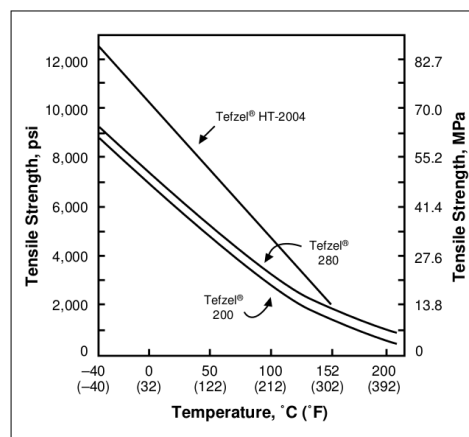
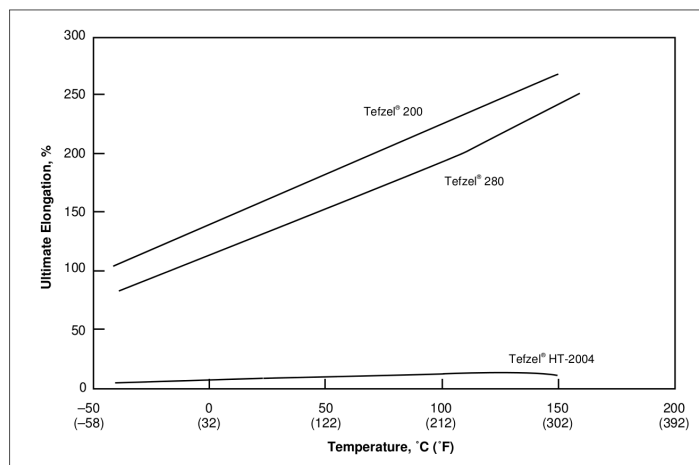


Figure 6.6: Yield stress and strain versus temperature performed by Moritz [15]



(a)



(b)

Figure 6.7: Test curves from DuPONT<sup>TM</sup> [54]: (a) tensile strength vs. temperature and (b) ultimate elongation vs. temperature

The experiments of Moritz [15] demonstrate that with temperature raise the yield stress decreases and the plastic behavior became more evident. These results are shown in figure 6.6.

Figures 6.7(a) and 6.7(b) highlight the dependence of the material behavior on the temperature. The results of interest are those of the Tefzel®200. Figure 6.7(a) demonstrates the decrease of the tensile strength as the temperature increases. For the ultimate elongation the value increases as the temperature increases.

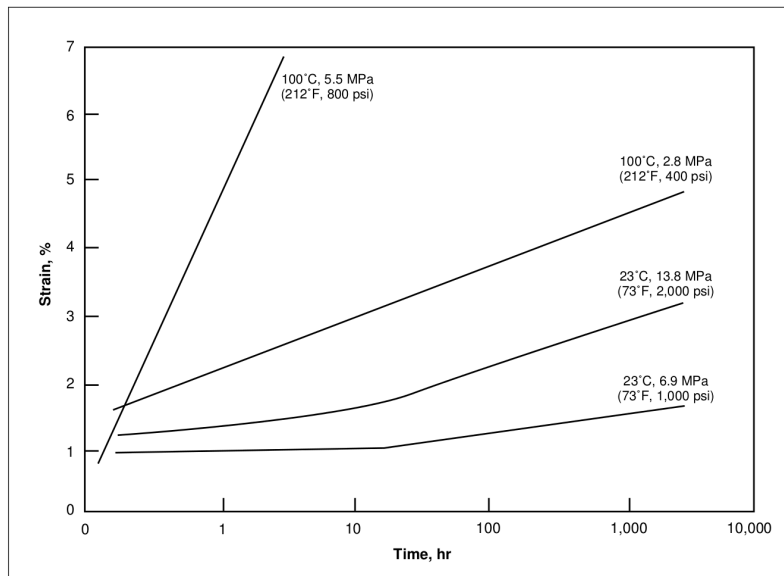


Figure 6.8: Creep test in DuPONT™ Tefzel 200 Flexural [54]

Figure 6.8 presents the creep test for Tefzel®200 for two values of temperature (+23°C and +100°C). It is observed that creep deformation increases with temperature.

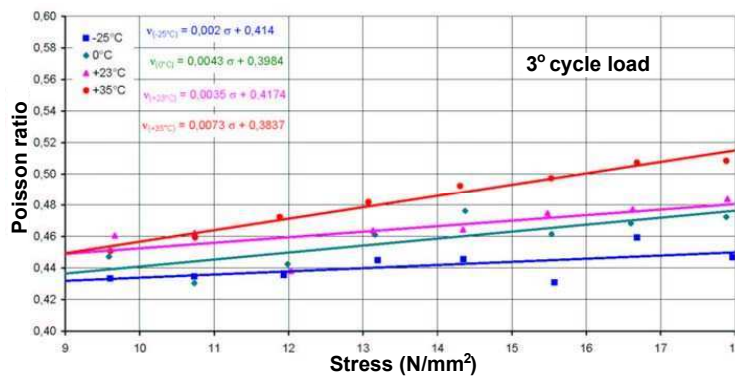


Figure 6.9: Poisson ratio versus stress for different values of temperature (source: Moritz [15])

The dependency of the Poisson ratio with stress for different values of temperature is shown in figure 6.9. For low temperatures the Poisson ratio can be con-

sidered constant, but for higher temperatures the variation of the Poisson ratio with stress should be considered.

## 6.2 Uniaxial and biaxial test by ETFE-foils

Based on the results and tests described in the previous section, numerical models based in finite element method are developed to fit the material parameters for the constitutive model of ETFE.

The mesh used for the uniaxial and biaxial tests is a rectangular membrane presented in figure 6.10. This mesh has 441 nodes and 400 quadrilateral linear elements. In figure 6.10 are presented the boundary conditions and the applied loads for this model. These examples are symmetric, therefore one quarter is modeled. The material properties are presented in table 6.1. These properties were extracted from the work of Galliot and Luchsinger [53]. The von Mises yield criteria is used in the elastoplastic model and a bilinear curve is used in the plastic phase due to the significant change in the hardening modulus observed experimentally.

The analysis is carried out with the arclength control and an equivalent nodal force is applied on the both edges.

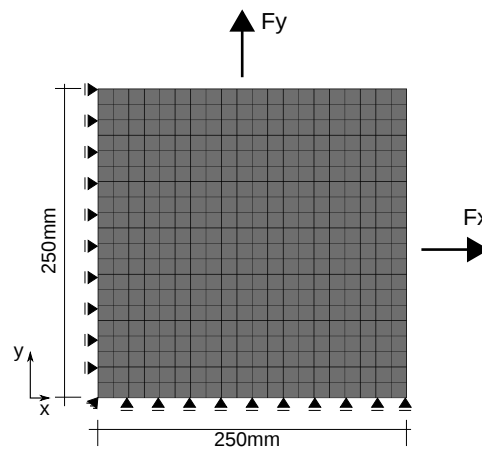


Figure 6.10: Mesh, geometry and boundary conditions for the biaxial test

Table 6.1: Material properties of ETFE-foils

Young's modulus ( $E$ )	1100MPa
Poisson ratio ( $\nu$ )	0.43
First yield stress ( $\sigma_{y_1}$ )	16MPa
First hardening modulus ( $K_1$ )	160MPa
Second yield stress ( $\sigma_{y_2}$ )	27MPa
Second hardening modulus ( $K_2$ )	80MPa

### 6.2.1 Uniaxial test

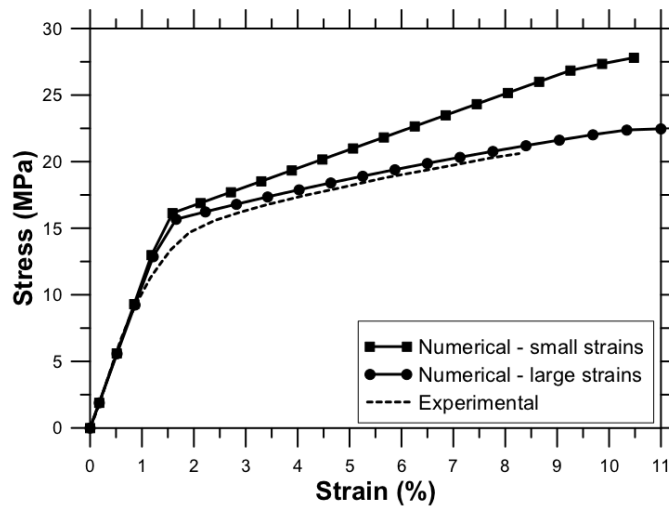


Figure 6.11: Stress versus strain for small and large strains

For the uniaxial test the force in the x direction ( $F_x$ ) is set to zero and the force in the y direction is incrementally increased. The results of the uniaxial test for large and small strains are presented in figure 6.11. The results are the same for small and large strains in the elastic phase, because the strains are still small. The difference in the results for small and large strains are large as expected once the small strains range has been largely exceeded.

### 6.2.2 Biaxial test

The biaxial test is analyzed for two load path with ratios: 2:1 and 1:1. In the case of proportion of 2:1, it was applied the double of the force in the y direction. The results for the numerical models are shown in figures 6.12 and 6.13. In both figures it is observed that the result with large strain model are closer to the experimental data. The difference between the results for small strains and large strains are also noticeable as the uniaxial test showed previously.

These results show the importance of considering large strains in the formulation for this type of material.

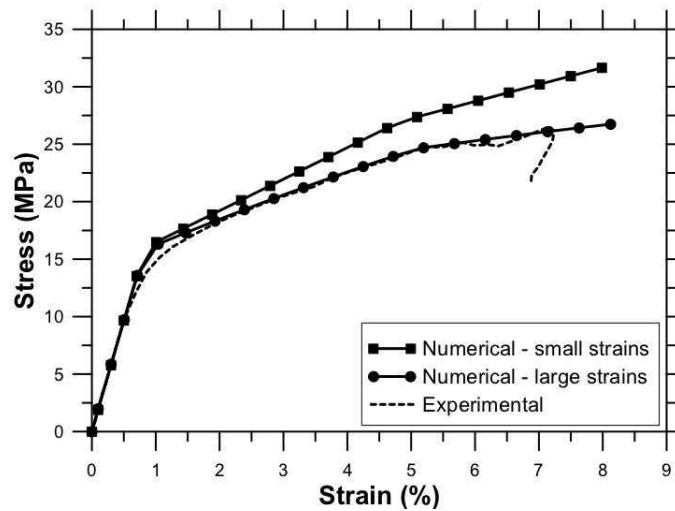


Figure 6.12: Stress versus strain for experimental results and numerical results with small and large strains for the biaxial loading in the proportion of 1:1

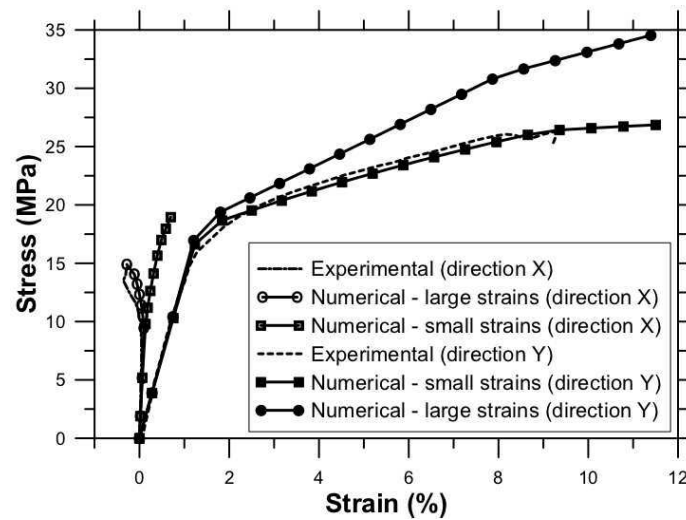


Figure 6.13: Stress versus strain for experimental results and numerical results with small and large strains for the biaxial loading in the proportion of 2:1

### 6.3 ETFE-Foil modeled with PD-NURBS

This example shows the application of PD-NURBS presented in chapter 4 to model a material making use of the available experimental results. The experimental results used to generate the NURBS surfaces are those of the biaxially loaded ETFE-foil under two loading programs ratios of applied force: 1:1 and 2:1 presented in the work of Galliot and Luchsinger [53]. The available experimental data is not enough to generate good NURBS surfaces. In order to obtain a point cloud data necessary for the generation of the NURBS surface data points based on the von Mises elastoplastic material formulation will be used. Figure 6.14 shows the experimental data points represented by the filled circles and the artificial ones by

hollow squares. In this figure the gap between the points of the experimental test is observed. With this data points, NURBS surfaces in principal directions for stress and strain are generated and figure 6.15 shows the NURBS surface in conjunction with the experimental data points.

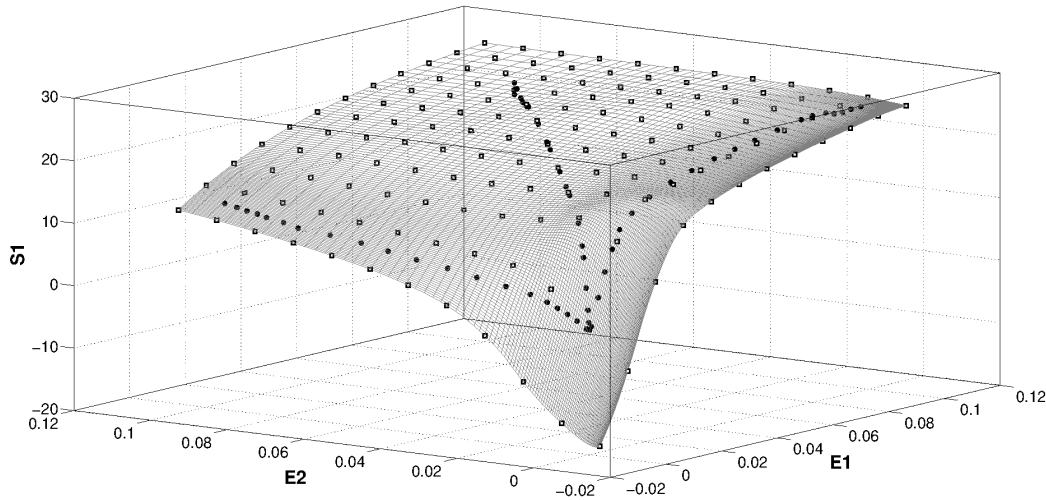


Figure 6.14: NURBS surface with experimental data

There is a dependence of the material model formulation with the size of the NURBS surfaces, in other words, input strains outside the NURBS surface, do not generate output stress results. In these regions artificial data is used to supply the stresses and strains information.

In figure 6.15 is observed that the experimental data points are on the NURBS surfaces.

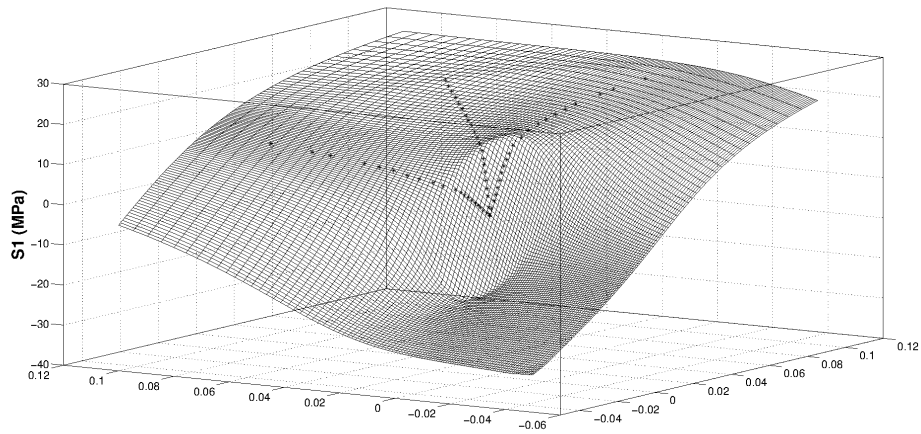
The test is carried out for two load ratios 1:1 and 2:1 as it was presented in the previous section. Geometry and mesh are the same used in the previous example.

### 6.3.1 Results

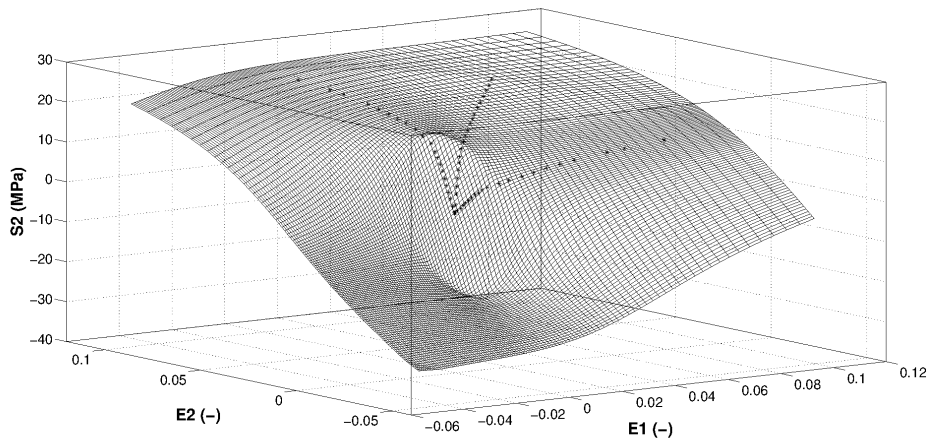
For both load ratios, the results are compared with the experimental results of Galliot and Luchsinger [53]. Table 6.2 shows the relative error of the numerical model with PD–NURBS material for stress and strain results. The error is calculated taking the experimental results as reference based on the following

$$Error = \frac{NURBS \text{ result} - Experimental \text{ result}}{Experimental \text{ result}} \cdot 100 \quad (6-1)$$

Table 6.2 shows that the error with the PD–NURBS material for the biaxial test for load ratios of 1:1 and 2:1 is small compared to the experimental results. We



(a)



(b)

Figure 6.15: NURBS surfaces of stress and strain in principal directions for von Mises material: (a) stresses in direction 1 and (b) stresses in direction 2.

Table 6.2: Relative error of biaxial test for the PD–NURBS material

		Error (%)			
Biaxial 1:1		Biaxial 1:1			
Strain	Stress	direction 2		direction 1	
		Strain	Stress	Strain	Stress
0.42	1.99	0.95	0.32	1.57	1.63

can also conclude that the PD–NURBS material model is suitable for the present membrane tests.

## 6.4 Burst test

Schiemann [84] and Galliot and Luchsinger [53] carried out experiments that consist in the inflation of an initially flat circular membrane, called burst test.

The burst test was performed with samples of ETFE-foil and were clamped in a bubble inflation test device between an aluminium plate and an aluminium ring. Air was injected between the aluminium plate and the foil, resulting in a spherical deformation. Tests were performed at room temperature, which corresponds to about 23 °C. The pressure in the bubble was recorded with a digital pressure sensor and the deformation of the bubble was measured with a 3D digital image correlation system.

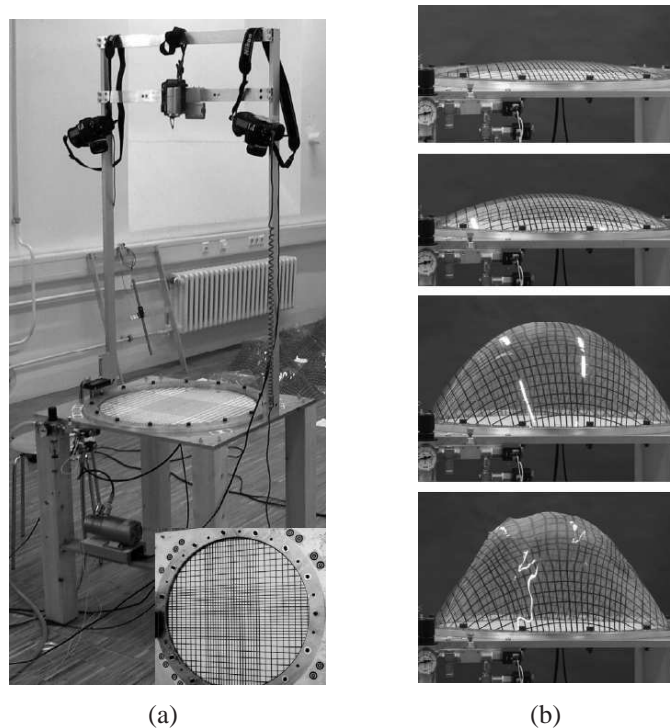


Figure 6.16: (a) Burst test and (b) deformation process (source: Schiemann [84])

The specimens tested by Schiemann [84] have a 53 cm radius and  $200\mu\text{m}$  thickness. Figures 6.16(a) and 6.16(b) show the apparatus for the experimental analysis and the deformation process of the burst test.

The burst test of specimen V28 from Schiemann [84] was carried out at a constant strain rate of 2.5%/min.

A finite element model is developed to compare with the results of the burst test of specimen V20 of Schiemann [84]. Figure 6.17 shows the mesh, geometry and boundary conditions used in the numerical model. Due to symmetry one quarter of the circular membrane is modeled.

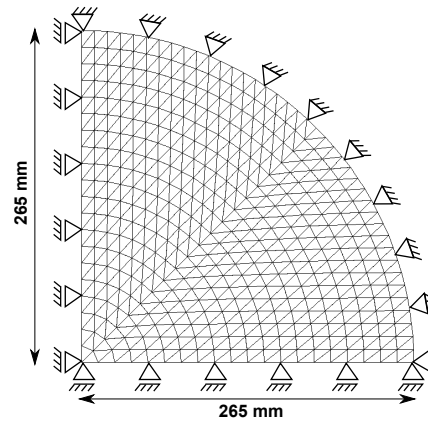


Figure 6.17: Geometry, mesh and boundary conditions for the burst test performed by Schiemann

A comparison for linear and quadratic triangular elements is carried out, in order to evaluate the results for both elements. The mesh is composed of 800 triangular elements for both linear and quadratic. The number of nodes is 441 for linear and 1681 for quadratic. The linear triangular element (T3) has 3 nodes and 1 Gauss integration point. The quadratic triangular element (T6) has 6 nodes and 3 Gauss integration points. Figure 6.18 presents the results of pressure versus displacement results for linear and quadratic triangular membrane elements. These results are the same for T3 and T6, therefore the linear triangular element is chosen to be used in these analysis due to the faster performance.

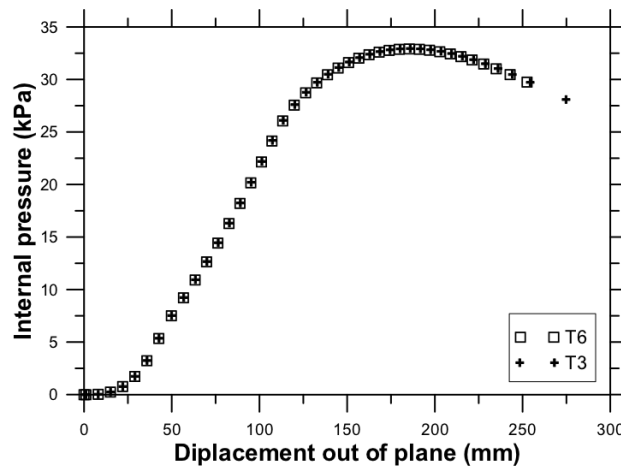


Figure 6.18: Pressure versus displacement results for the specimen V28 [84]; linear (T3) and quadratic (T6) triangular membrane elements.

Based on the previous analysis of the uniaxial and biaxial tests of ETFE-foil in section 6.2, the elastoplastic material model with von Mises yield criteria is considered in the numerical analysis. The properties of the ETFE are extracted from the work of Schiemann [84] and are presented in table 6.3. A bilinear curve is used in the plastic phase due to the significant change in the hardening modulus observed

Table 6.3: Material properties of specimen V28

Young's modulus ( $E$ )	417MPa
Poisson ratio ( $\nu$ )	0.45
First yield stress ( $\sigma_{y1}$ )	14MPa
First hardening modulus ( $K_1$ )	120MPa
Second yield stress ( $\sigma_{y2}$ )	32MPa
Second hardening modulus ( $K_2$ )	30MPa

experimentally.

#### 6.4.1 Results

The analysis is carried out with the cylindrical arc-length method. Figure 6.19 shows the pressure versus displacement curve for two different values of the step length, 60 and 100.

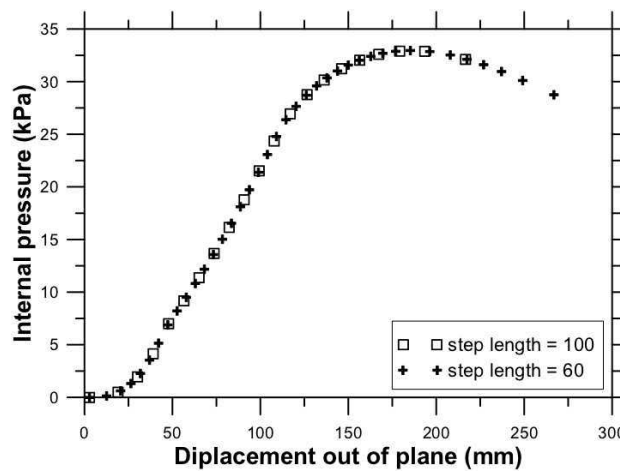


Figure 6.19: Pressure versus displacement results for the specimen V28 [84]; step length of 60 and 100.

Table 6.4 presents the global convergence rate of the displacement residuum at the critical pressure for the adopted step length values (60 and 100). A small difference in the convergence is observed.

Figure 6.20 presents the plot of applied pressure versus the out of plane displacements for specimen V28, obtained with numerical analysis for the elastoplastic material model with large and small strains. The results obtained with the numerical model with large strains demonstrate its suitability to model this experiment. On the other hand, the numerical model with small strains is valid only in the first steps of the analysis where the strains remain small.

Table 6.4: Global convergence of the displacement residuum at the critical pressure for step length values of 60 and 100.

	step length	
	60	100
1	2.023e+01	2.166e+01
2	3.261e+00	2.850e+00
3	8.899e-02	4.937e-02
4	6.604e-05	4.682e-05
5	3.684e-09	2.359e-08

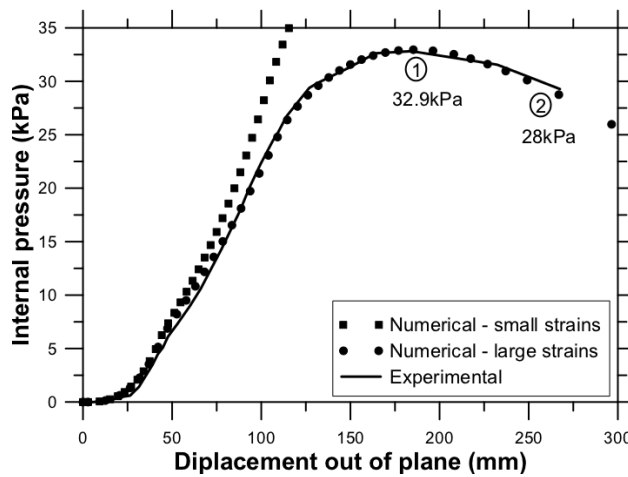


Figure 6.20: Pressure versus displacement results for the specimen V28 [84]; large strain, and small strain material models.

The deformed configuration of both the experimental and numerical analyses with large strains are presented in figure 6.21. The results are shown for two stages of the applied load, which are indicated in figure 6.20 with the numbers 1 (32.9kPa) and 2 (28kPa).

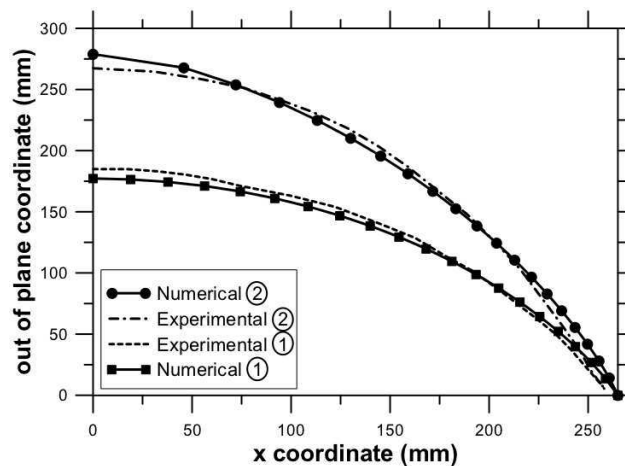


Figure 6.21: Deformed configuration of the specimen V28 [84] and numerical model with large strains for pressure states 1 and 2.

Figure 6.22 shows the stress versus strain curve in the y direction for the numerical analysis with large strains. States 1 and 2 are the same depicted in figures 6.20 and 6.21. Comparing figures 6.20 and 6.22 the non proportionality of pressure and stresses is noticeable. After the critical pressure, the strains increase mightily.

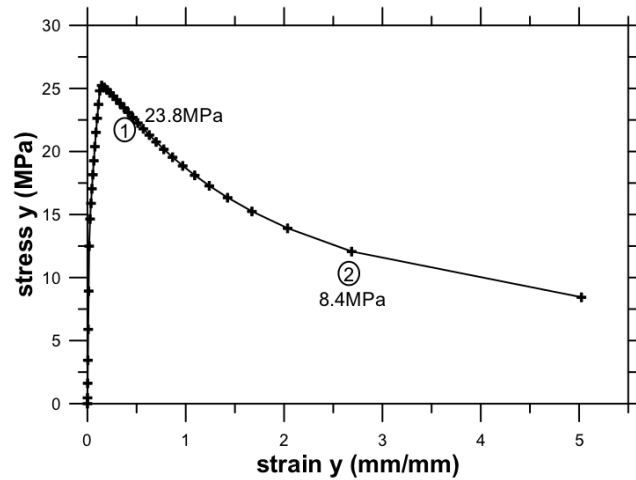


Figure 6.22: Stress versus strain curve in y direction

Deformed configurations of the inflated circular membrane in three dimensions are shown in figure 6.23. The two states 1 and 2 are again represented.

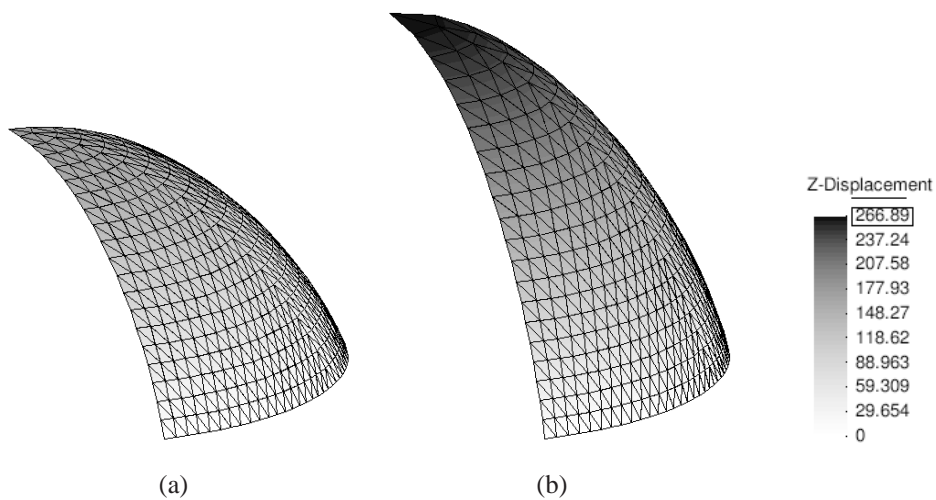


Figure 6.23: Deformed inflated circular membrane with the out of plane displacement: (a) point 1 and (b) point 2

### 6.5 Air cushion with single and double chamber

The objective of this example is to examine the response of the pneumatic structure considering the pressure–volume coupling formulation presented in chap-

ter 5.

The single chamber air cushion composed by two membranes was analyzed in the studies of Jarasjarungkiat [75] and Linhard [31]. This structure is extended here to a double chamber with a membrane in the middle. Cushion compositions for single chamber and double chamber are represented in figures 6.24(a) and 6.24(b), respectively.

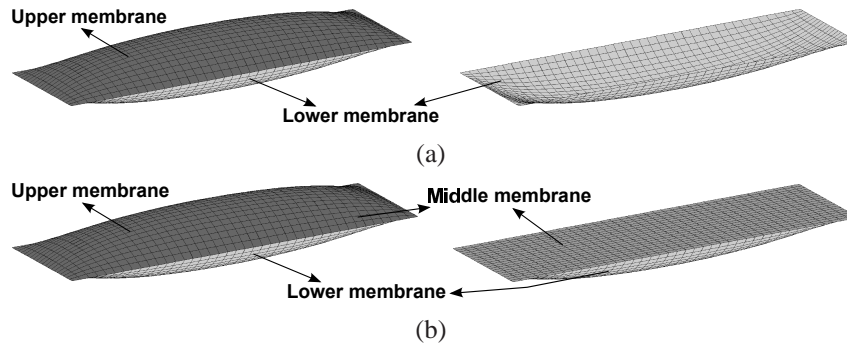


Figure 6.24: Undeformed cushions: (a) upper and lower membranes of single chamber cushion and (b) upper, middle and lower membranes of double chamber cushion

Rectangular cushion dimensions are 6 meters length and 3 meters width. Linhard [31] applies formfinding analysis to this cushion with internal pressure of  $400\text{Pa}$  and prestress of  $0.89\text{Pa}$ . Jarasjarungkiat [75] presents a static analysis after the formfinding process applying an external force in the center of the cushion distributed on 9 elements. The cushion dimensions and the configuration after the formfinding stage are illustrated in figure 6.25.

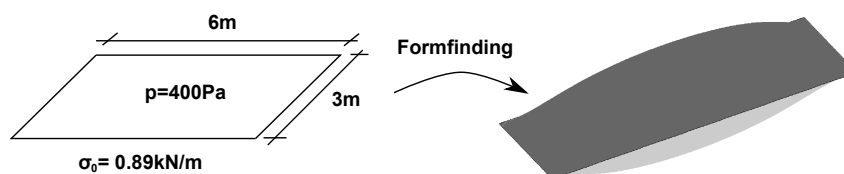


Figure 6.25: Cushion dimensions and formfinding shape

The analysis is carried out first for the formfinding stage followed by the static stage. Both single chamber and double chamber cushion considering the influence of the pressure–volume coupling are analyzed and presented.

Load control is used in the static stage and the force is applied up to  $2.38\text{kN}$  in 10 steps.

### 6.5.1 Single chamber cushion

The single chamber cushion is composed by two membranes, an upper membrane and a lower membrane. The initial internal pressure is 400Pa and the initial volume is  $9.173m^3$ . The results for the deformation under external load and volume versus internal pressure are presented in figures 6.26 and 6.27, respectively.

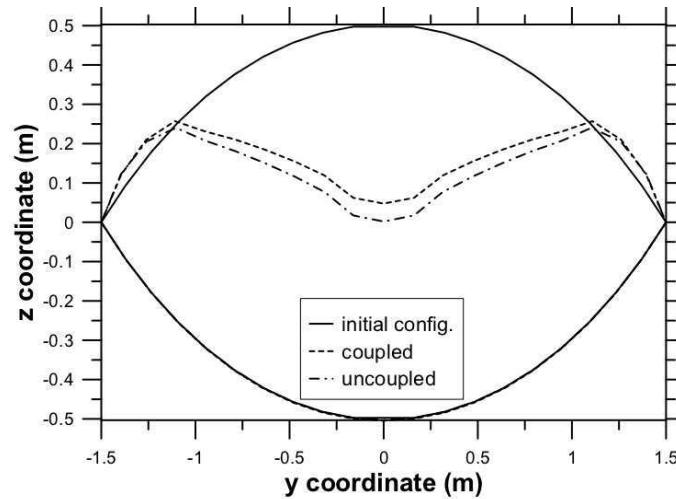


Figure 6.26: Single chamber cushion deformation under external load

The deformation of the single chamber cushion (figure 6.26) is for a load of  $2.38kN$ . Considering the pressure–volume coupling the membrane deforms less compared to the case without pressure–volume coupling. This is in agreement with the Boyle–Mariotte law. The analysis with pressure–volume coupling leads to internal pressure raise as the enclosed volume decreases resulting in smaller displacements compared to the analysis without coupling.

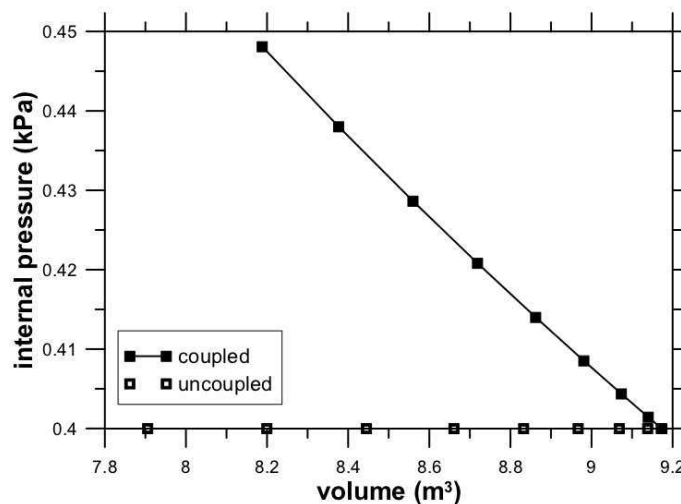


Figure 6.27: Volume versus internal pressure for the single chamber structure

Volume versus internal pressure results for the single chamber cushion are presented in figure 6.27. In this plot it is observed that by the analysis with no coupling the internal pressure remains unchanged and the volume decreases more when pressure-volume coupling is presented.

## 6.5.2

### Double chamber cushion

The double chamber cushion under consideration has one additional membrane between the upper and lower membranes (three membranes). The initial pressure and initial volume for each chamber are respectively: 400 Pa and  $4.58m^3$ . The results for the deformation under external load and volume versus internal pressure are presented respectively in figures 6.28 and 6.29.

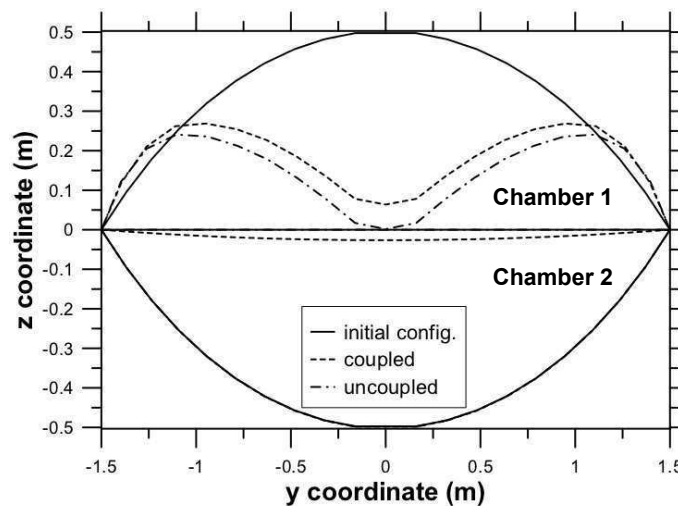


Figure 6.28: Two chambers deformation under external load

The deformation results of the double chamber cushion correspond to an external load of  $2.38kN$ . The results for the upper membrane with no coupling are the same as the ones obtained in the analysis of the single chamber structure. Figure 6.28 shows that the middle membrane in this case doesn't introduce any change. On the other hand the middle membrane presents some deformation by the coupled analysis .

The internal pressure of chamber 1 by the uncoupled analysis remains unchanged, as expected. Chamber 2 has no influence in the results in this case. The internal pressure of chamber 2 for the coupled analysis increases as the volume decreases and follows the curve of chamber 1.

Figure 6.30 presents the out of plane displacement versus applied load results in the center node of the cushions for the single and double cushion structure with and without pressure–volume coupling. The uncoupled analysis for single and

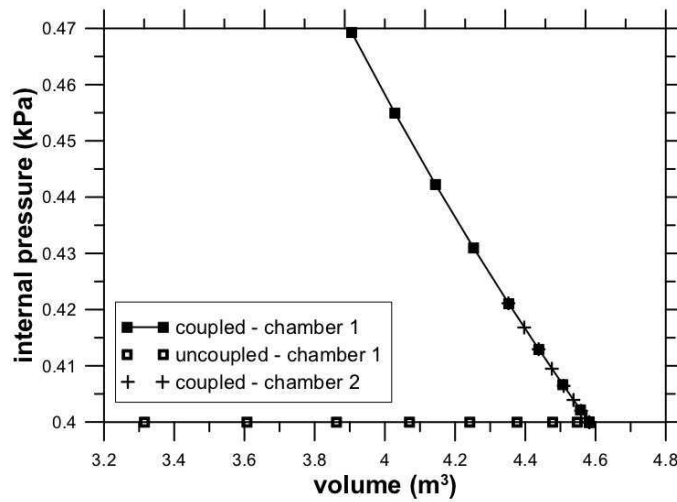


Figure 6.29: Volume versus internal pressure for two chambers

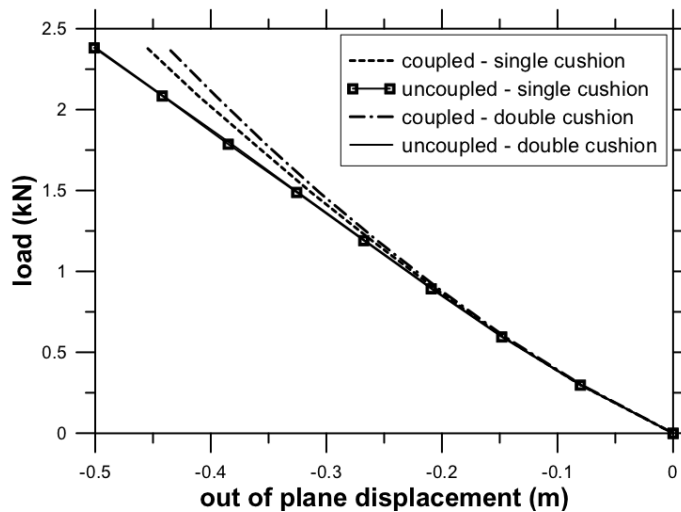


Figure 6.30: out of plane displacement versus load

double cushion present the same results. The displacements of the double cushion obtained by the coupled analysis are smaller than those of the single cushion.

## 6.6

### Lyon confluence cushion ©seele

This example explores a pneumatic structure in use. It is a place of leisure and shopping center in Lyon (France) and seele is the company responsible for the cushion roof. According to seele [85] the roof structure is supported by 36 m high steel columns which carry the trussed steel arches of circular hollow sections. Between these, further similar arches run in two diagonal directions. On plane the roof is therefore a network of rhombuses and triangles which determine the shapes of the two-layer foil cushions from seele. The cushions are framed by aluminium

sections on all sides which are fixed to steel channels. Figure 6.31 shows the overall structure.



(a)



(b)

Figure 6.31: Lyon confluence cushion structure: (a) top view and (b) bottom view

The analysis is carried out for one cushion due to the deformation between the rigid metal frames that surround the cushions and the membrane. In other words, the analysis can be carried out for each cushion separately. Cushion data such as geometry, membrane properties, internal pressure, and applied load was provided by seele. The geometry of the triangular cushion is presented in figure 6.32.

Table 6.5 presents the material properties of the triangular cushion. The PD–NURBS material model is used for the membrane material. Since no experimental data was available for this material, the NURBS surfaces are generated based on the elastoplastic material with von Mises yield criteria. Its good accordance with the ETFE–foil response was shown in the previous examples.

Table 6.5: Material properties of the ETFE-foil

Young's modulus ( $E$ )	900MPa
Poisson ratio ( $\nu$ )	0.45
First yield stress ( $\sigma_{y1}$ )	15MPa
First hardening modulus ( $K_1$ )	72MPa
Second yield stress ( $\sigma_{y2}$ )	21MPa
Second hardening modulus ( $K_2$ )	40MPa

The internal pressure of the cushion is  $0.3kN/m^2$  and the ETFE-foil thickness is  $250\mu m$ . The external load is a uplift wind pressure of  $1.5kN/m^2$ .

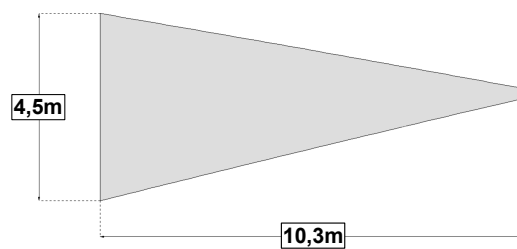


Figure 6.32: Geometry of the triangular cushion

The analysis is carried out for load control of the triangular cushion with and without cutting pattern generation. The meshes for both cases are presented in figure 6.33 and the flat patterns in figure 6.34.

Formfinding analysis is performed, for the internal pressure of  $0.3kN/m^2$  and prestress of  $3.32kN/m^2$ , before the cutting pattern analysis. In other words the work flow for the present pneumatic analysis is first the formfinding, second the cutting pattern generation, and third the static analysis.

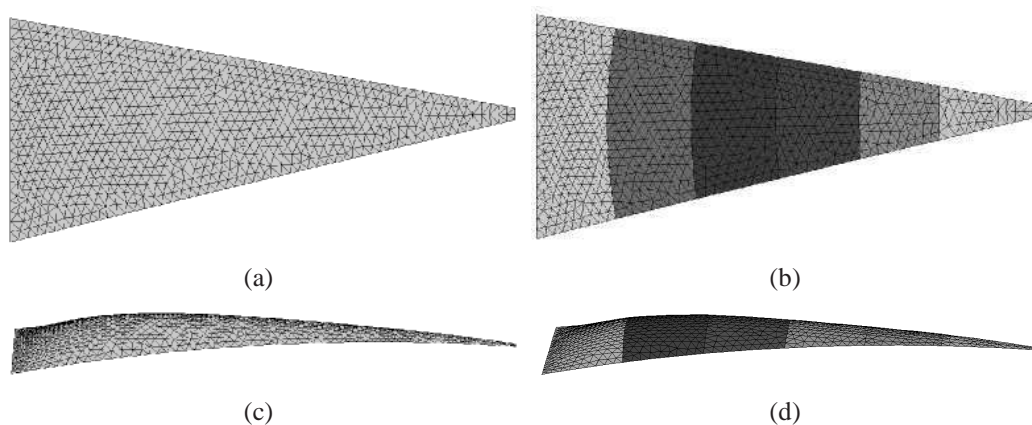


Figure 6.33: Mesh of the cushion structure: (a) and (c) without cutting patterns (b) and (d) with cutting patterns.

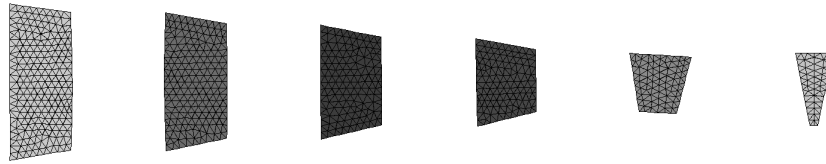


Figure 6.34: Flat patterns of the triangular cushion.

### 6.6.1 Results

The static analysis has two stages. First, the inflation of the cushion is performed. Second, the external wind load is applied. The static analysis is run for both with and without cutting patterns. In each case the effect of the pressure–volume coupling is presented. Figure 6.35 shows the von Mises stress distribution results with pressure–volume coupling. Attention is given to the stress distribution on the membrane. Without cutting pattern generation the maximum stress is located on the edge of the membrane depicted with the letter A in Figure 6.35(a). On the other hand for the case with cutting pattern generation the maximum stress is located in the middle of the membrane depicted with the letter B in Figure 6.35(b).

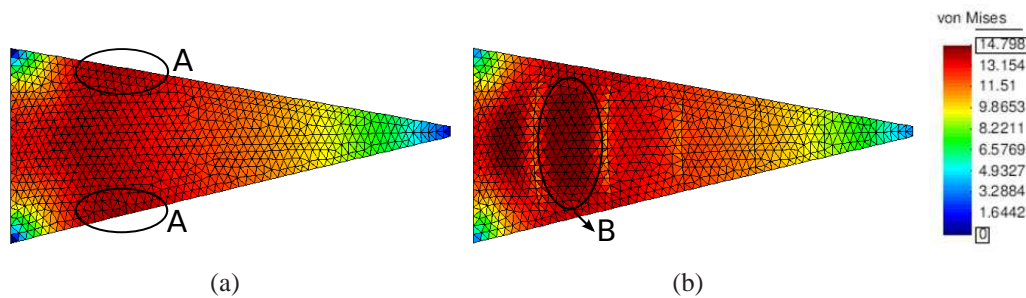


Figure 6.35: Von Mises stress distribution on the cushion structure with pressure–volume coupling: (a) without cutting patterns, (b) with cutting patterns.

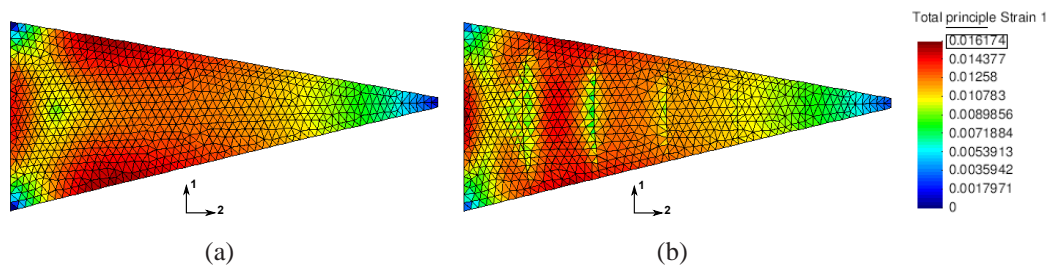


Figure 6.36: Strain in principal directions 1 on the cushion structure with pressure–volume coupling: (a) without cutting patterns, (b) with cutting patterns.

Figures 6.36 and 6.37 present the results of strain in principal directions for the cases with and without cutting pattern generation considering pressure–volume coupling. The distribution of strain values in principal direction 1 is similar for

both with and without cutting pattern generation but in the pattern unions the strain values are smaller. On the other hand the strain distribution in principal direction 2 is different in both cases. The case with cutting pattern presents larger strain values on the surface while the case without cutting pattern has compressive strains on the membrane border.

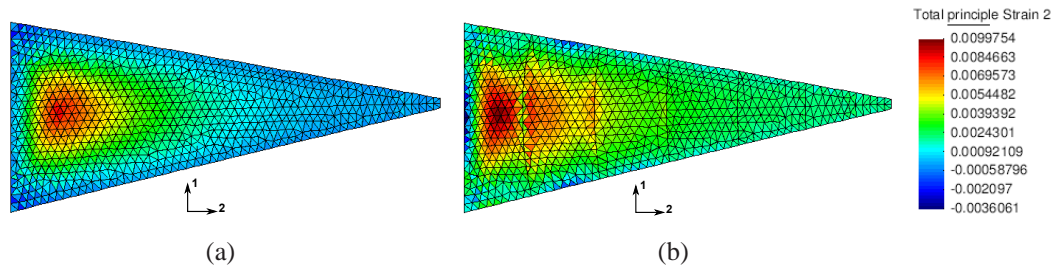


Figure 6.37: Strain in principal directions 2 on the cushion structure with pressure–volume coupling: (a) without cutting patterns, (b) with cutting patterns.

Table 6.6: Maximum result values for the triangular cushion

		von Mises stress (MPa)	Strain (%)		Stress (MPa)	
			direc. 1	direc. 2	direc. 1	direc. 2
cp <sup>a</sup>	coupled	14.798	1.61740	0.99754	16.560	14.652
	uncoupled	14.877	1.65050	1.05760	16.639	14.753
n-cp <sup>b</sup>	coupled	14.346	1.55840	0.85644	16.551	13.931
	uncoupled	14.553	1.60250	0.87532	16.796	14.229

<sup>a</sup>cp = with cutting pattern <sup>b</sup>n-cp = without cutting pattern

Table 6.6 presents the maximum result values obtained in the four analysis. Wind uplift pressure reduces the internal pressure in the analysis considering the pressure–volume coupling resulting in smaller values for stress, strain and displacements.

Larger values are observed for cushion analysis with cutting pattern generation due to the accumulation of tension on the strip unions.

The largest values were found by the analysis with cutting pattern generation, without pressure–volume coupling.

Figures 6.38 and 6.39 present the stress versus strain results for the triangular cushion with and without cutting pattern generation. Figure 6.38 shows the results with PD–NURBS material and figure 6.39 shows the results for the elastoplastic with small strain. For each case the coupled and uncoupled of pressure–volume models are considered. For the case with cutting pattern generation the last two steps are in the plastic region. This is observed through the slope change of the curve. On the other hand the case without cutting pattern for both coupled and uncoupled are in the elastic region. The results for the coupled analysis present smaller values.

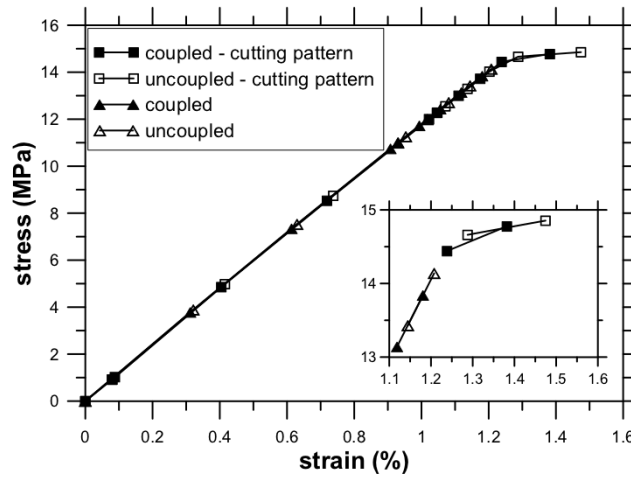


Figure 6.38: Stress versus strain for triangular cushion with PD-NURBS material.

Figure 6.40 shows the results of internal pressure versus volume for the triangular cushion with and without cutting pattern. The coupled and the uncoupled analysis are run for both cases. The uncoupled results are represented with the hollow symbols and both have constant internal pressure. The results of the coupled analysis for both cases with and without cutting pattern, have the same curve slope. However, the difference in the initial geometry, due to the cutting pattern, results in a difference in the initial volume. Last would be to say that seele used cutting pattern made of 8 strips per layer instead of 6 as the investigated model based upon.

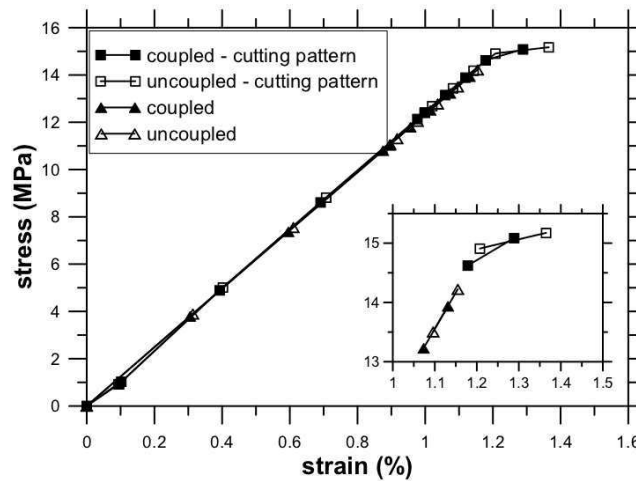


Figure 6.39: Stress versus strain for triangular cushion with elastoplastic material with small strains.

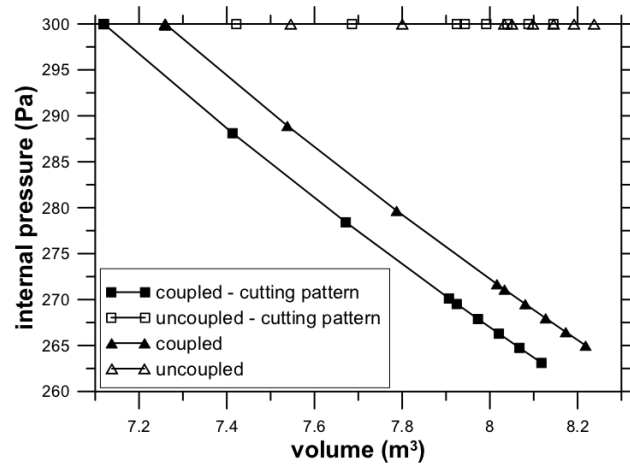


Figure 6.40: Internal pressure versus volume for the triangular cushion.